Z. Phys. D 30, 291–306 (1994)

ZEITSCHRIFT
FÜR PHYSIK D

Dielectronic recombination of lithium-like Ar^{15+}

S. Schennach[3,*], A. Müller[1,*], O. Uwira[1,*], J. Haselbauer[*], W. Spies[1,*], A. Frank[1,*], M. Wagner[*,], R. Becker[2], M. Kleinod[2], E. Jennewein[***], N. Angert[3], P.H. Mokler[3], N.R. Badnell[4,†], M.S. Pindzola[5]**

[1] Institut für Strahlenphysik, Universität Stuttgart, D-70569 Stuttgart, Germany
[2] Institut für Angewandte Physik, Universität Frankfurt, D-60054 Frankfurt, Germany
[3] Gesellschaft für Schwerionenforschung (GSI), D-64291 Darmstadt, Germany
[4] Department of Physics & Applied Physics, University of Strathclyde, Glasgow G4 0NG, UK
[5] Department of Physics, Auburn University, Auburn, AL 36849, USA

Received: 21 December 1993 / Final version: 11 February 1994

Abstract. Dielectronic recombination (DR) of $Ar^{15+}(1s^22s)$ ions was studied in a single-pass merged–beams experiment at the UNILAC (universal linear accelerator) of GSI. Absolute recombination rates and cross sections were measured for electron-ion center-of-mass energies from 0 to 580 eV. A number of Rydberg states formed by DR with $2s \rightarrow 2p$ ($\Delta n = 0$) and $2s \rightarrow 3\ell$ ($\Delta n = 1$) core excitations and even individual terms in the $1s^23\ell3\ell'$ configuration could be resolved. Theoretical calculations of DR cross sections are in good overall agreement with the data. In the calculations for $\Delta n = 0$ transitions, effects of electric fields have to be included to reproduce the magnitude of the measured DR rates at the limit of the $2p_{1/2}n\ell$ and $2p_{3/2}n\ell$ Rydberg series. Discrepancies between theory and experiment are observed at the series limits of the $(1s^23\ell n\ell')$ Rydberg series.

PACS: 34.80.Kw

1. Introduction

Electron-ion collisions are fundamental processes, which play an important role wherever ionized matter occurs. Data on electron-ion collision processes are needed for the modeling and understanding of astrophysical and laboratory plasmas [1] such as the solar corona, the discharge in a tokamak, or the spark produced by an intense laser when it hits solid material. Among a variety of other electron-ion processes, recombination is particularly interesting both from an applied point of view and as a testing ground for our theoretical understanding of atomic structure and atomic collision phenomena. Due to experimental difficulties inherent in the colliding-beams techniques, direct measurements of electron-ion recombination cross sections and rates have been carried out only since a few years [2, 3] . During this time enormous progress has been achieved, both in the experiments and theory [4].

Much of the present interest in the field of electron-ion recombination is related to the construction and operation of heavy ion storage rings. In particular, ion beam cooling by interaction with a cold electron beam raises the question of losses due to recombination processes. Experimental studies of electron-ion recombination are needed to understand more about the loss mechanisms. They can also serve to diagnose the effectiveness of ion beam cooling. An ion storage ring with an electron beam cooling device in itself provides an excellent tool to study recombination processes and to obtain data which are useful for plasma applications.

A free electron and an ion A^{q+} can recombine by radiative recombination (RR)

$$e + A^{q+} \rightarrow \left[A^{(q-1)+}\right]^* + h\nu \,, \tag{1}$$

where the excess energy is carried away by a photon in a direct process. After RR the captured electron can be in a highly excited (bound) state and hence further radiation will be emitted until the electron is in the lowest possible level.

The recombination can also proceed in a resonant manner

$$e + A^{q+} \rightarrow \left[A^{(q-1)+}\right]^{**} \rightarrow \left[A^{(q-1)+}\right]^* + h\nu \,, \tag{2}$$

where the excess energy released by the capture of the electron is used up by the excitation of a core electron within the ion. This so called resonant recombination or dielectronic capture can only occur, if the kinetic energy of the projectile electron matches the difference E_i - E_f of total binding energies of all electrons in the initial and final states of the ion. Inevitably, dielectronic capture produces a multiply excited autoionizing state, which can decay by the emission of photons

$$\left[A^{(q-1)+}\right]^{**} \rightarrow \left[A^{(q-1)+}\right]^* + nh\nu \tag{3}$$

and thus stabilize the reduced charge state of the ion. The whole two-step process of resonant recombination followed by stabilization via photoemission is termed dielectronic

* *Previous affiliation:* Institut für Kernphysik, Justus-Liebig-Universität, Giessen, Germany
** Deceased
*** *Previous affiliation:* Institut für Angewandte Physik, J.-W.-Goethe-Universität, Frankfurt, Germany
† *Previous affiliation:* Department of Physics, Auburn University, Auburn, AL 36849, USA

recombination (DR). Usually, however, electron emission from the intermediate resonant electron-ion complex

$$\left[A^{(q-1)+}\right]^{**} \rightarrow A^{q+} + e \tag{4}$$

is much more likely than photoemission so that the compound disintegrates again into the original constituents.

The situation becomes more complex when the intermediate state is so highly excited that cascades of stabilizing transitions are possible. Then radiative transitions are in competition with autoionization in more than one intermediate step, which makes it difficult to follow the path of radiative stabilizations through all possible decay channels.

With increasing electron densities, another recombination mechanism becomes important: In the three-body recombination process

$$e + e + A^{q+} \rightarrow A^{(q-1)+} + e \ , \tag{5}$$

one of the two electrons carries away the excess energy released by the recombination of the other electron and the ion. This process is important at very low center-of-mass energies of electrons and ions. In this paper we exclude the discussion of recombination processes at very low energies and rather deal with two-body DR collisions only.

Much of the present activity in the field of electron-ion recombination has been devoted to lithium-like ions. These ions provide a relatively simple electronic structure and correspondingly can be treated more easily by theory than ions with a more complex structure. Moreover, beams of such ions are usually free of metastable components which would make the interpretation of results difficult. Pioneering experiments with the lithium-like ions B^{2+}, C^{3+}, N^{4+}, and O^{5+} were carried out at Oak Ridge by Dittner, Datz and co-workers [3, 5]. With a better electron beam target and vastly improved energy resolution the ions C^{3+}, N^{4+}, O^{5+}, F^{6+}, and Si^{11+} were studied in Aarhus by Andersen and co-workers [6, 7]. All these experiments were restricted to the $\Delta n = 0$ transitions of the $(2s)$ electron

$$e + A^{q+}(1s^2 2s) \rightarrow \begin{cases} A^{(q-1)+}(1s^2 2p_{1/2} n\ell) \\ \\ A^{(q-1)+}(1s^2 2p_{3/2} n\ell) \ , \end{cases} \tag{6}$$

where $n\ell$ characterizes a high Rydberg level into which the incident electron is captured.

The first measurement providing data also for $\Delta n = 1$ transitions of the $(2s)$ electron where carried out at the Heidelberg test storage ring (TSR) with Cu^{26+} ions [8]. In these experiments an ultimate resolution of 0.1 eV was reached at the lowest relative energies of electrons and ions. This resolution is even slightly better than that in the Aarhus experiments. (Of course the finite longitudinal temperature of the electron beam always leads to an increasing energy spread in the merged-beams experiments as the center-of-mass energy is raised.)

The most highly charged lithium-like ions studied so far with respect to DR and RR are Au^{76+} [9, 10] and U^{89+} [11]. These experiments were carried out at the experimental storage ring ESR of GSI. Due to the technical difficulties in the detuning of the electron energy in the cooling device, these measurements have had to be restricted to $\Delta n = 0$ core transitions (see (6)).

The present measurements were carried out in a single-pass merged-beams experiment at the UNILAC of GSI. An extremely dense cold electron beam target was employed providing an energy spread as low as 0.2 eV at the lowest energies in the center-of-mass frame of electrons and ions studied. DR with both $\Delta n = 0$ and $\Delta n = 1$ transitions of the $(2s)$ core electron of Ar^{15+} was investigated. The experimental results are compared with theoretical calculations of cross sections for DR. Effects of electric fields in the collision region are taken into account.

After a rather comprehensive description of the experimental apparatus and its components, the data acquisition and the evaluation of experimental cross sections and rates are then presented in detail. The theoretical methods and assumptions are next briefly summarized and the results of theory and experiment are finally compared and discussed.

2. Experimental arrangement

For studying recombination of highly charged ions and free electrons we have set up a single-pass merged-beams experiment [12, 13] at the UNILAC of GSI in Darmstadt (see Fig. 1). Briefly, the ion beam from the accelerator enters the experiment through narrow (variable) slits with typically 1mm × 1mm aperture. It is charge analyzed by a 22.5° deflection magnet and the ions with selected charge state are then transported to the electron target [14 – 18]. A second identical magnet analyzes the charge states of ions emerging from the target. Recombined ions are detected by a position sensitive detector. The parent ion beam is collected in a wide Faraday cup.

The first section of the apparatus serves to decouple the moderate vacuum (some 10^{-6} mbar) in the beam transport line of the UNILAC from the ultra-high vacuum in the experiment. Low background-gas pressure is necessary in order to reduce electron capture by the highly charged ions in ion-atom or ion-molecule collisions. The pressure reduction is primarily accomplished by separating the two vacuum regimes with a long, narrow tube. The whole system is pumped by 5 turbomolecular pumps with a nominal pumping speed of about 500ℓ/s each, two titanium sublimation pumps, and two NEG (non-evaporable getter) pumps. In addition, the electron target itself with its inner bore cooled to liquid helium temperature, provides an efficient cryo-pump with a surface of about 1 m^2. Already in front of the charge-state selection magnet a typical pressure in the order of $1 \cdot 10^{-10}$mbar is achieved.

The ion beam from the UNILAC is bent about 135° by 6 identical magnets before it enters the present setup through the entrance slits. Each of these magnets is provided also with entrance and exit slits so that a relative ion-beam energy resolution of better than 10^{-4} is achieved. Before the narrow tube, that limits the gas flow from the accelerator beam line into the ultra-high vacuum in the experimental setup, a second pair of movable slits is installed which set a

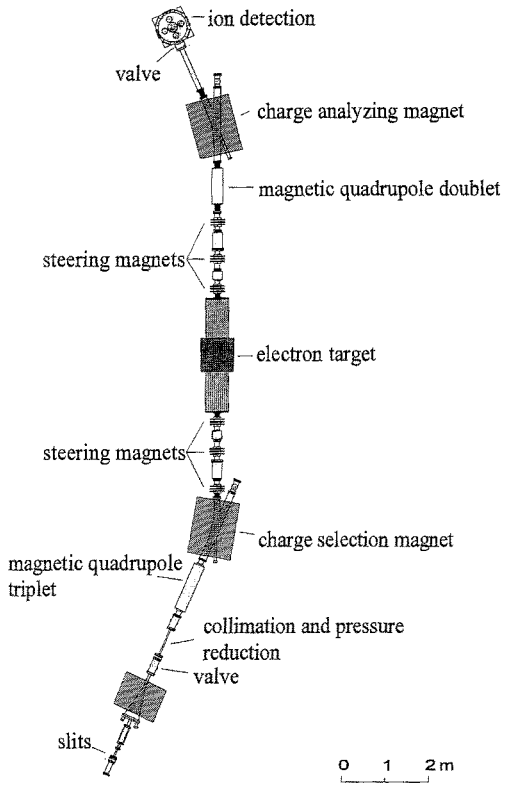

Fig. 1. Schematic overview of the entire experimental merged-beams setup at the UNILAC of GSI. For details, see text

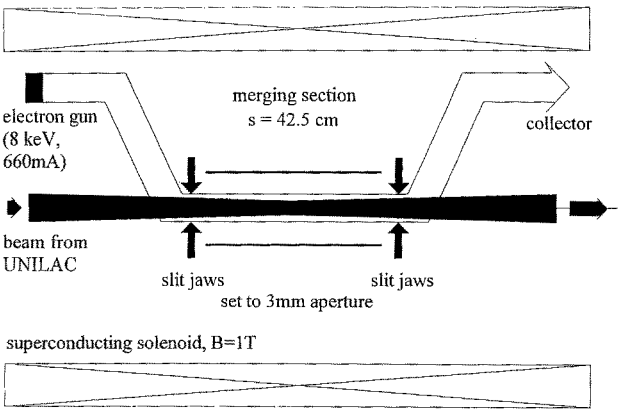

Fig. 2. Schematic diagram of the present merged beams experiment designed for the heavy ion accelerator UNILAC of GSI, Darmstadt. The electron gun is inside the homogeneous field of a superconducting solenoid. Bending the electron trajectories onto the ion beam axis is accomplished by additional tilted elliptical windings embracing the solenoid. Two sets of slits are indicated by solid arrows. These slits can be moved in small steps leaving a nearly circular aperture between 3 mm and 10 mm diameter. The electron beam is 3 mm in diameter. The electric potential of the interaction volume is defined by the voltage applied to a pair of parallel metal strip electrodes. These electrodes are separated by 30 mm. They are schematically indicated by the two solid lines below and above the electron-ion interaction region. In reality, these strips are parallel to the plane of the present figure, i. e. mounted left and right when viewed in the electron beam direction

final limit of 2π mm mrad to the emittance of the beam. Using beam steerers and focussing elements, located upstream from the experiment, the beam current through the collimation slits is optimized. A magnetic quadrupole triplet in front of the charge selection magnet then focuses the ion beam to a spot size of 1 mm diameter in the center of the electron target. The maximum ion beam diameter inside the electron beam (at the given emittance) is 2 mm. Thus, the ion beam is completely contained inside the electron beam, which has a diameter of 3 mm. The interaction region of electron and ion beams is sketched in Fig. 2.

The electron target facility provides a dense electron beam serving as a target for the incident ion beam. The maximum density is $n_e = 10^{10}$ cm^{-3}. This value is attained for an electron energy of 8 keV. The electron beam is immersed in a strong axial magnetic field, which is produced by a superconducting solenoid. Tilted elliptical windings enclosing the solenoid provide transverse magnetic field components which serve to merge and separate the electron beam and the ion beam. The transverse field components are strong enough (up to 15 % of the maximum field obtained in the middle of the solenoid, i.e. up to 0.15 T), that they bend not only the electron beam but also influence the ion beam. The resulting deflection would not allow transport of the ions from the target to the detector chamber without correction of the trajectory. For the same reason the ion beam cannot be injected into the electron beam directly on the symmetry axis. The ion beam rather has to be injected into the target at a given angle with respect to the main solenoid axis and it has to be injected from a given position displaced up to several millimeters from the axis. Therefore the ion beam trajectory has to be adjusted both upstream and downstream from the electron target. These requirements are met by employing six rotatable magnetic steerers, three in front of the electron target and three behind, which compensate for the deflection of the ion beam caused by the transverse magnetic field components in the target.

A second (analyzing) magnet with a 22.5° deflection angle is then used to separate the parent ion beam from those ions which have changed their charge downstream from the charge selection magnet (see Fig. 3). The recombined (and also the parent) ions are focused into the detection chamber by a magnetic quadrupole doublet positioned in front of the analyzing magnet. The detector chamber contains a rather wide (20 mm × 70 mm) and deep tantalum Faraday cup with electric supression of secondary electrons. It collects the primary ion beam (charge state q). The detector for the recombined ions (charge state $(q-1)$) consists of a chevron arrangement of two 40 mm diameter microchannel plates and a resistive anode. The detector is mounted inside a cylindrical housing whose front opening is covered by a thin aluminum foil (20 μm thick). This foil shields the detector from low-energy stray electrons, ions and photons.

The energetic ions from the accelerator do not change their energy when they pick up a free electron in the electron target. They can easily penetrate the entrance foil and are detected by their production of secondary electrons in the foil and on the surface of the first microchannel plate. When the detector is used without the entrance foil, in order to detect low energy particles, the total operating voltage is about 2300 V (with 1900 ± 100 V across the stack of the two microchannel plates). With highly charged ions of several MeV/u energy, the detector voltage can be reduced to 1500 V for obtaining the same pulse heights. Apparently, the production of secondary electrons is so efficient that lit-

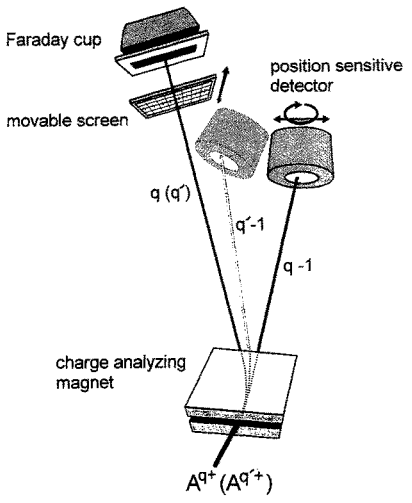

Fig. 3. Schematic view of the separation and the detection of parent and recombination-product ions. The wide Faraday cup is fixed to the rear flange of the detector chamber. The position sensitive microchannel-plate detector (PSD) can be moved ± 25 mm in the plane of the different ion beams (perpendicular to the axis of the beam pipe) and thus accomodate different ratios $q/(q-1)$ of parent and product ion charge states. Moreover, the PSD can be rotated around a vertical axis perpendicular to the plane of the two beams. This can be used to reduce the width of the non-sensitive PSD area (the "dead area") as seen by the recombined ions. Finally, the PSD can also be retracted from the plane of the two beams. In the figure the situation is shown for two different parent ion charge states q and q' with $q' > q$ and hence for two different positions of the PSD. The sensitive PSD surface is shown as a shaded area. The ceramic screen serving as a beam viewer can be moved into and out of the parent ion beam

tle amplification is needed. This also indicates that there is a very low probability for an ion to produce no secondary electron arriving at the microchannel plate front surface, and hence the ion detection probability must be very close to 100 %.

The detector is supplied with a resistive anode, i.e. the collector for electron avalanches emerging from the rear surface of the second microchannel plate is covered with a resistor material conducting the collected charge to 4 different corners of the resistive layer. Thus, the resistive anode provides 4 signal pulses for every incoming ion. The pulse heights of these four signals allow us to obtain the position of the incoming ion with a precision of about 0.2mm. Hence, it is possible to monitor the beam position in the detector chamber while the ion beam is tuned for optimum quality of transmission through the experimental apparatus. This is an important diagnostic tool, which helps to find the correct settings of the ion optical elements. In fact, optimizing the ion beam for an experiment is extremely difficult because of the necessary compensation of the transverse magnetic field components in the electron target and the related beam handling. This difficulty is ultimately caused by the requirement of high density and low temperature in the electron target: the transverse magnetic field component, $B_\perp$, has to be strong with respect to the longitudinal component, $B_\parallel$, (here $B_\perp/B_\parallel = 0.15$) to limit the length of the merging section; $B_\parallel$ has to be strong to keep the transverse temperature $T_\perp$ of the electron beam low; hence, $B_\perp$ reaches up to $0.15\,T$ in the present arrangement.

The range of parent ion charge states which can be studied by the present experiment is limited by the geometrical separation of parent and product ion beams in the detector chamber. The beam pipe between the magnet chamber and the detector chamber limits the acceptance of a pair of beams emerging from the analyzing magnet to a maximum angular separation of less than 3 °. This geometrical limitation together with the specific data of the magnet (i.e. a bending radius $\rho = 2730$ mm, effective path length of an ion trajectory inside the magnet $2\ell \approx 108$ cm as well as distance between the effective magnetic field edge and the detector plane $L = 1785$ mm) allows detection of both the product ions and the parent ions in the detector chamber provided the parent ion charge state is $q \geq 12$.

With increasing ion charge state q the separation $D_{q,q-1}$ of parent and product ions at the position of the single particle detector becomes smaller, approximately with the relationship $D_{q,q-1} = 890\ \mathrm{mm}/q$. When the parent ion is very highly charged, the product ion beam may be separated only a few millimeters and then the non-sensitive area between the microchannel-plate detector and the Faraday cup becomes the limiting factor for recombination experiments. The limiting distance between the parent and product beams -assuming a beam diameter of 5mm- is 30mm, which results in a maximum charge state $q = 29$. However, the ion beams, being only few millimeters wide, do not require a 40 mm diameter detector area. By rotating the detector around a vertical axis (perpendicular to the plane defined by the parent and product beams), the effective detector area can be reduced. For a rotation by 75 ° the effective width of the detector area is about 10mm instead of 40mm and at the same time the width of the non-sensitive area is also reduced. Because of the geometry of the detector housing, a minimum distance D between the parent and product ion beams of 18 mm is required. As a consequence, the maximum parent ion charge state, allowing recombination experiments with $q \rightarrow q-1$, is about $q \leq 50$ in the present setup. These numbers depend on the beam diameter in the detector plane. A beam diameter of 5 mm is assumed.

Between the limiting cases, different charge states can be accomodated by moving the detector with an ultra-high vacuum manipulator in the horizontal direction until its position matches the beam requirements and the fixed position of the (wide) Faraday cup. A new detector geometry which reduces the dead area around the sensitive surface is under development and will allow the access of higher charge states q. With the initial charge state $q = 15$ in the present experiment the separation and the collection of the parent and product ion beams were easy.

3. The electron target

Compared to gas or even solid targets, a beam of charged particles typically provides particle densities which are many orders of magnitude smaller [19]. Counting rates and the

signal-to-background ratio in electron-ion collision studies can be enhanced by designing electron beams with high current densities and a geometry which allows enhanced interaction lengths. These features can be provided by electron cooling devices [20] in storage rings, where electron beams with densities of the order of 10^7 cm^{-3} are merged with circulating ion beams over a length of up to 2.5 m. This solution involves the use of toroidal magnetic guiding fields to bend the electron beam in and out of the ion beam.

A different approach was used by Dittner et al. [5, 21] in their experiments on DR. They used a convergent electron beam from a spherical cathode with electrostatic focussing. The electron beam was further compressed by an axially increasing magnetic field so that electron densities of the order of 10^9 cm^{-3} could be achieved. The ion beam entered the electron beam through a hole in the cathode and was thus merged with the electron beam. The disadvantage of that approach was the increase of the transverse temperature in the compressed electron beam, and hence, the energy resolution of electron-ion collision experiments was rather limited. Compared to storage-ring cooler devices the energy spread in the Oak Ridge electron beam target was increased by more than a factor 10. The question arising from that result is whether it would be possible to combine high particle density in the electron beam with low transverse and longitudinal beam temperatures. A solution to this twofold demand is given by the electron target used in the present experiments.

If the low transverse temperature $T_\perp$ of the electron beam given by the temperature of the cathode ($kT_\perp \approx 0.1$ eV, where k is Boltzmann's constant) is to be conserved, the electron beam must not be compressed. It has to be guided in a very homogeneous axial magnetic field and the acceleration has to be in a certain functional dependence on the magnetic field along the axis. The conditions for proper operation are known as Pierce's resonance focusing [22] and provide a beam which does not become radially heated. The requirement for a certain current density in the electron beam relates the strength of the magnetic field to the square root of the acceleration voltage. The maximum electron current density (saturation current density) that can be drawn from an oxide impregnated tungsten cathode is about 10 A/cm^2. For such a high value the necessary magnetic focusing field strength has to be 1 T, homogeneous to within 10^{-4}, to conserve the radial energy spread given by the cathode temperature. An electron beam with these features was realized for the present experiments.

The configuation of the electron gun designed for the production of a cold electron beam with a maximum density is shown in Fig. 4. Calculated equipotential lines and electron trajectories are displayed together with the electrode geometry. The calculation includes the space charge fields produced by the electron beam as well as the external magnetic field of the solenoid. It is apparent from this calculation that the electron beam has a homogeneous current density and, very important, is absolutely parallel.

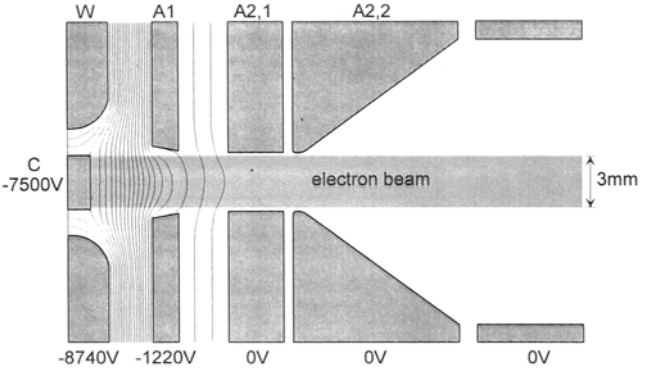

Fig. 4. Schematic view of the electron gun. The electrodes are indicated as shaded areas. Voltages (with respect to ground potential) applied to the electrodes are indicated for the high-perveance mode. The abbreviations are: C, cathode; W, Wehnelt electrode; A1, first anode; A2,1 and A2,2, splitted second anode. A part of the subsequent drift tube is also shown. Calculated electron trajectories[23] as well as equipotential lines, obtained by iteratively solving the Poisson equation and the resulting equations of motion, are displayed as solid lines. The space charge of the electron beam as well as an axial magnetic field of $1.03\,T$ are included in the calculations

The electron gun was designed by employing the SLAC electron optics program [23]. The perveance of this electron gun is $0.95 \cdot 10^{-6}$ A/V$^{3/2}$, providing a current of 660 mA at 8 keV. With a beam diameter of 3 mm this corresponds to the maximum achievable current density of 10 A/cm^2. The maximum electron density is 10^{10} cm^{-3}, which exceeds the density of electron coolers in storage rings (or of other similar target devices) by more than two orders of magnitude. At the same time a low radial temperature is maintained. A numerical analysis of the potential distribution inside the electron beam and of the trajectories of single electrons provides information about the expected energy spread in the electron beam. The potential depression inside the electron beam, i.e. the potential difference between the center and the edge of the electron beam due to its space charge, is expected to be ≈ 110 V . Since the electrons are fixed to their magnetic field lines, however, they gain little radial energy from the electric space charge field. The result obtained from the electron optics calculation yields a radial temperature of the electron beam lower than 0.3 eV at the maximum electron density.

The space charge potential differences in the electron beam only have an effect in the longitudinal direction, i.e. electrons at the center of the beam have about 100 eV less energy than those at the edge of the beam. In the transition from the laboratory frame to the electron-ion center-of-mass frame this longitudinal energy spread is very much reduced by the kinematics of the merged beams experiment. In other words, the longitudinal energy differences in the electron beam at 8 keV correspond to a low value of $kT_\parallel$ in the range of some 10^{-3} eV. For further reduction of the longitudinal temperature $T_\parallel$, a second mode of electron target operation was provided. Such a mode with a perveance a factor of 10 less than that for the high density operation required a third anode to maintain resonance focusing. By space charge compensation as well as by lower electron currents, space charge effects are reduced accordingly and hence the longitudinal temperature of the beam can be expected to be much

lower. The present experiments were carried out with the electron gun in the high perveance mode and with Ar^{15+} ions of 5.96 MeV/u, corresponding to an electron energy of 3270 eV in the laboratory frame for matching the electron and ion velocities. In this regime the electron densities were below 40 % of the maximum value and hence, space charge effects were also considerably reduced from those expected for the maximum density. The experiments discussed below had a radial electron temperature which corresponds to $kT_\perp \approx 0.2$ eV.

The requirements for the magnetic field needed to confine the electron beam were fulfilled by a superconducting solenoid. The cold bore of the solenoid magnet serves as the vacuum vessel for the electron beam target. This has the advantage of very efficiently cryopumping the interaction region. Different from the design of other devices of this kind, e.g. the cooler devices in ion storage rings, the present arrangement does not use toroidal magnetic fields for merging and separating the electron and ion beams [18]. Instead, a straight solenoid with elliptical windings for the transverse magnetic field components is used. The electron gun and the collector are placed 22.5 mm off-axis but fully immersed inside the homogeneous magnetic field. A distance of 45 cm is required to merge the electron beam with the ion beam. The interaction length is 42.5 cm, so that a homogeneous field region of about 1 m length is required. The necessary homogeneity of the magnetic field can be achieved by the use of properly distributed single current loops. An overall length of the solenoid of about 2 m is sufficient to meet these requirements with the collector placed in the decreasing fringe field.

A superconducting solenoid with windings consisting of thin Nb Ti wire provides the required magnetic field strength of 1 T with a homogeneity of 10^{-4} for the production of the high-density, low-temperature electron beam. The length of the solenoid is 1.9 m, with the open bore of the cylindrical vacuum vessel 150 mm in diameter. The electrical current necessary to achieve 1 T is 105 A.

Transverse magnetic field components, necessary for merging and separating the electron beam and the ion beam, are provided primarily by oppositely energized elliptical coils consisting of 6×48 windings with a pitch of 4/3. Additional elliptical windings with different pitches as well as additional annular windings are used to compensate the return fields and provide the desired field configuration. The accuracy of the magnetic field configuration was checked at various stages of the production process. Trim windings were designed and installed at these steps in order to compensate inaccuracies of the actual windings. The final result of this procedure is a magnetic field with less than 10^{-4} variation in the interaction region [18].

The superconducting solenoid is surrounded by two thermal shields which are cooled by a closed-cycle refrigerator system to less than 20 K and 60 – 80 K, respectively. All components of the target surrounding the merging section are thermally grounded to the 60–80K shield. The water-cooled collector is completely thermally insulated. The electron gun and collector are optically shielded from the inner bore of the solenoid, which is at 4.2 K. This is accomplished with chevron baffles, that allow for sufficient pumping. All inner parts of the electron target are attached to tubes connected to the 60 – 80 K shield. The tubes provide a very rigid and stable structure. The correct alignment is accomplished by using thermally isolated glass stems to position the entire structure inside the precisely machined magnet bore.

Secondary electrons produced at the collector or by ionization of residual gas particles need to be prevented from oscillating through the interaction region. The collector is therefore kept at a slightly positive potential with respect to ground. Thus the total power deposited is up to 5 kW. The primary electrons are therefore collected in a long narrow wedge-shaped gap between two water-cooled copper plates in order to reduce the heat load per unit area.

An important feature of the electron target is the ability to check electron and ion beam positions and diameters during an experimental run. This is accomplished by two sets of electrically isolated variable slits just in front of and behind the interaction zone of the two beams. These slits are 42.5 cm apart and also define the length of the merging section of the two beams (see also Fig. 2). By measuring electron or ion currents to the slit jaws it is possible to tune the ion beam for complete overlap with the electron beam, i. e. the ion beam can be set and controlled to be completely contained inside the electron beam. These slits are particularly useful for finding the optimum settings of the ion beam steerers used to compensate the deflection by the transverse magnetic fields of the electron target.

4. Experimental procedures

For the present experiment an ion energy of 5.96 MeV/u was chosen, with a beam of Ar^{10+} at the desired energy available from the UNILAC accelerator. A debuncher cavity of the UNILAC was used to reduce the energy spread of the incident ion beam (or increase the ion current for given tight settings of the magnet slits). The ions were then passed through a stripper foil and thus Ar^{15+}, i.e. lithium-like argon, could be obtained with a fraction of about 25 % of the total beam current. The beam transport line upstream from the target contains 7 magnets not including the septum magnet after the UNILAC. These magnets, together with slit systems in between, allowed the preparation of an ion beam with low relative energy spread (better than 10^{-4}). The time structure of the ion beam for the present experiment was characterized by a macropulse length of 5 ms and a repetition period of 20 ms. Within the macropulse, the RF accelerator provides beam pulses at a frequency of 27 MHz and a micropulse duration of about 2 ns. This duty factor of 25 % had to be considered in estimating dead times of the detector, since the instantaneous counting rate of recombined ions is 4 times higher than the average.

The tightly collimated ion beam must be transported through the experiment into the final Faraday cup. The available beam diagnostic elements, which have to be compatible with the ultra-high vacuum requirements, consist of several movable Faraday cups and ceramic screens that could be inserted at appropriate positions along the ion beam line. Energetic ions produce a lightspot on the surface of the ceramic screens which can be monitored by a television camera while the ion beam is "on" (and produces safety-relevant neutron radiation). The two pairs of slits inside the electron target are installed in such a way, that they may touch the electron beam when they are adjusted to a 3 mm aperture. Therefore, an ion beam focused through the centered slits, set to 3 mm diameter or less, is completely contained inside the electron beam. When the ion beam has the desired shape and position inside the electron target, the superconducting solenoid including the elliptical windings is energized in small steps. As the magnetic field is increased at each step, the two sets of beam steerers have to be adjusted to keep the ion beam within the interaction volume, defined by the slits, and to also keep it on the final Faraday cup. When the magnetic field strength necessary for the desired electron energy is reached and the ion beam traverses the 3 mm slits without losses, the slits are opened (by stepping motors with very small gear ratio allowing very precise positioning) and the electron gun is switched on. The electron beam is always reproducible in its position and the ion beam does not move once the ion optics and the collimation slits are properly set. Thus, complete overlap of the two beams can be checked and assured.

The electron-ion center-of-mass energy, E_{cm}, in the collision region is changed by variation of the electron laboratory energy, E_e, while the ion beam energy, E_i, is fixed. E_e can be varied in two ways. One technique is to keep the interaction volume at a constant potential and change the cathode potential (as well as the potentials of the other electrodes, according to the requirements of resonant focusing and collection of the electrons at a fixed power level in the collector). The other technique is to vary the potential U_{int} of the interaction volume and keep everything else unchanged. The potential U_{int} is determined by the voltage (with respect to ground), applied to a set of two parallel strip electrodes separated by 30 mm. Centered between the two strips are the interacting beams. At the high densities possible in the electron beam, the space charge of the electrons produces a considerable potential difference U_{sc-} between the plates and the electron beam center. For the actual geometry, $U_{sc-} \approx 5.7 \cdot 10^{-8} n_e \mathrm{V\,cm^3}$, which is typically about 300 V for the present experiment. This means that the electron beam center is at a potential 300 V more negative than the drift electrodes.

In the experiment, we tried both positive and negative potentials (with respect to ground) on the strip electrodes. The energy resolution determined by the widths of resonances from DR processes was lowest when U_{int} was less than $-100\,\mathrm{V}$. For scanning E_{cm} we chose, therefore, a voltage range $-100\,\mathrm{V} \leq U_{int} \leq -500\,\mathrm{V}$. With the two sets of slits in front of and behind the interaction volume fixed at ground potential a trap for positive ions is formed in this mode of operation. Such ions are always produced by the electron beam in collisions with residual gas particles. The (slow and partially trapped) positive ions provide a positive space charge, which partially compensates the electron space charge. The experiment can be used to determine the electron energy in the interaction region provided the ion energy is known. The latter is continuously controlled by time-of-flight measurements and is therefore well known. When the electron velocity matches the ion velocity the recombination rate has a pronounced maximum. This is expected for radiative recombination for which the cross section diverges if E_{cm} goes to zero. Hence, the experiment provides a signal from which the instantaneous electron energy at a given cathode voltage and for given U_{int} can be determined. From such measurements it could be inferred that slow ions compensate typically 70 % of the electron space charge. The effect of this compensation is a greatly improved energy resolution of the measurements. At the same time, the ions may produce additional background in the counting of recombined (fast) ions, which can quite easily be subtracted.

The voltage range $-100\,\mathrm{V}$ to $-500\,\mathrm{V}$ for U_{int} was covered with up to 1024 equidistant steps. Each voltage step was set by a computer via a 16 bit digital-to-analog converter (DAC) to a programmable power supply within the 15 ms pause after a macropulse of the accelerator. The power supply is fast enough to reach the desired voltage at less than 1 ms. Thus, 50 voltage steps could be made within one second so that one complete scan took only 200 s. By repeating scans many times, the desired level of statistical uncertainties of the numbers of counts per energy could be reached within typically a few hours.

The electron current I_e was measured both as an electrical current emitted by the cathode and a current measured on the collector. I_e is stable during the time intervals of about 5 ms of each individual energy step. The ion current collected by the Faraday cup was measured by a current digitizer whose output pulses were counted with a scaler. The single particle detector for the recombined ions is connected to an electronic unit providing a number of different signals which were recorded appropriately: A "rate" signal is available from a sum pulse taken from the resistive anode after amplification and fast discrimination. The dead time of this data channel is about 0.6 μs. In addition, the position information on the ion, incident on the detector, is available in two 1-byte words for the x- and y- directions. In order to keep the amount of accumulated data within a reasonable frame, only the 3 most significant bits were recorded for each of the two coordinates of each detected ion. In addition, the "data-ready" signal for each position signal of an ion was measured by a separate scaler. This channel has a dead time of 3 μs. The data taking time per energy step was also recorded.

At each voltage step, the electron current, the average parent ion current, the number of counts of recombined ions (both from the fast and the slow channel of the position electronics), the pulses from a constant-frequency pulser and a 8×8 position matrix are recorded as a function of the actual electron energy. The position information is stored in a

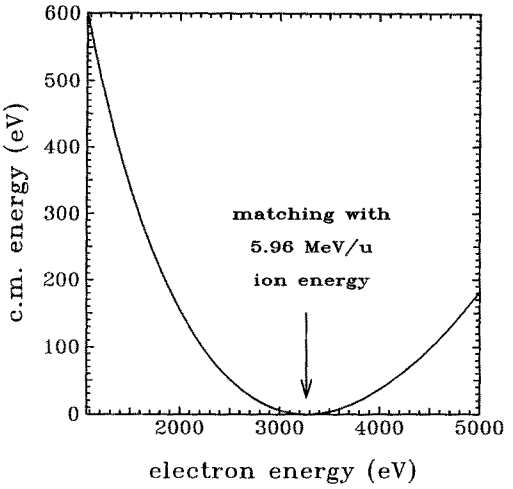

Fig. 5. Center-of-mass energy E_{cm} as a function of electron laboratory energy E_e for merged beams of electrons and 5.96 MeV/u Ar^{15+} ions. (see (7))

histogramming memory with an address space of 64 kB so that for each energy a position matrix of the detected ions is available. The other quantities are recorded in different spectra where the accumulated number of counts per energy step is available as a function of the electron energy.

The scalers and the histogramming memory were gated by a logic pulse obtained from an AND-gate which combines the macropulse of the accelerator with a "ready" signal of the computer used for controlling the experiment. Thus, data were only taken when the ion beam was on and the computer had completed it's controlling and data handling tasks, and, in particular, when the new voltage U_{int} was set.

5. Kinematics

When a beam of particles with rest mass m_1 and kinetic energy E_1 collides at an angle Θ with a beam of particles with rest mass m_2 and kinetic energy E_2, then the relativistic center-of-mass energy is given by

$$E_{cm} = [(m_1c^2 + m_2c^2)^2 + 2(E_1E_2 + E_1m_2c^2 + E_2m_1c^2 - \sqrt{E_1(E_1 + 2m_1c^2)}\sqrt{E_2(E_2 + 2m_2c^2)}\cos\Theta]^{1/2} - (m_1c^2 + m_2c^2) \quad (7)$$

For kinetic energies much smaller than the rest energies of the particles this formula can be reduced to the classical form of $E_{cm} = \mu(\mathbf{v_1} - \mathbf{v_2})^2/2$, where $\mu = m_1m_2/(m_1 + m_2)$ is the reduced mass, and $\mathbf{v_1}$ and $\mathbf{v_2}$ are the particle velocities in the two beams, respectively. At the present energies and velocities, the differences between the classical and the relativistic energies are at most a few eV. Nevertheless, the relativistic formula was used to determine E_{cm} in the present electron-ion recombination experiment. Figure 5 shows E_{cm} versus the electron energy E_e for merged electron and ion beams, i. e. $\Theta = 0°$. The specific ion energy is $E_i/m_i = 5.96$MeV/u corresponding to the actual situation in the experiment.

Near the region, where electron and ion velocities match, the electron energy has to be detuned considerably in order to access only a small range of electron-ion center-of-mass energies. This implies also that a rather big energy spread in the electron beam transforms to a small spread in E_{cm}. Clearly, a given E_{cm} can be realized by two different voltage settings in the electron beam. The ions can be faster or slower than the electrons for the same relative velocity. In the present experiment, a range 1100 eV $\leq E_e \leq$ 5150 eV was investigated. In order to span this range with the technique of scanning U_{int}, a number of scan measurements, each with a 400 V span in U_{int}, were carried out with different voltage settings on the electron gun fixed for each single scan measurement. The spectra obtained by this procedure were measured with overlapping energy regions and, hence, could be combined to one total spectrum.

6. Evaluation of cross sections

When electrons with a spatial density $n_e(\mathbf{r})$ and ions with a spatial density $n_i(\mathbf{r})$ interact in a volume τ via a cross section $\sigma(v)$, where $\mathbf{v}$ is the vector of relative velocity between the collision partners and $v = |\mathbf{v}|$ its absolute value, then the rate R of interactions is given by

$$R = \int_\tau \int_v n_e(\mathbf{r})n_i(\mathbf{r})\sigma(v)vf(\mathbf{v})\mathrm{d}^3v\mathrm{d}^3r \quad (8)$$

For the deduction of cross sections from measured counting rates R the spatial density distributions of the particles and the distribution function $f(\mathbf{v})$ of the relative velocities have to be determined. In the equation it has been assumed already that f is independent of the location $\mathbf{r}$. In electron-ion colliding beams experiments the integral over spatial density distributions is usually taken into account by introducing so called form factors [19]. In the present experiment the situation is somewhat simpler. The density $n_e(\mathbf{r})$ of the electrons is uniform in space with calculated variations of less than 5 % across the electron beam. The homogeneous magnetic guiding field for the electrons guarantees a constant electron beam diameter through the whole system (except inside the collector). The electron beam diameter can be checked by using the slits in the electron target. The measurements show a beam diameter of 3mm at both locations. This is the design value and is equal to the diameter of the cathode. Strongly inhomogeneous electron density could therefore only result from dead spots on the cathode emitting fewer electrons than expected. This is very unlikely, however, since the cathode was operated in the space-charge limited mode at energies where only one third of the maximum emission current density is required. The total electron current drawn from the cathode coincides with the design value and hence the emission from the cathode must be as uniform as predicted (otherwise the total current would be less).

With uniform electron density n_e, (8) can be simplified considerably since the two integrations are assumed to be independent of each other and $n_e(\mathbf{r})$ can be taken out of the integral. Integration over n_i just yields the number of ions present in the interaction volume. In case the ion beam is completely inside the uniform electron beam, this number is simply given by $I_i\ell_{eff}/(qev_i)$, where I_i is the electrical ion current, q the ion charge state, e the charge of an electron,

ℓ_{eff} the length of the interaction path, and v_i the ion velocity.

The integral over the velocity distribution $f(\mathbf{v})$ can be carried out separately by introducing a rate coefficient α. In plasma experiments, $f(\mathbf{v})$ is determined by the temperature of the plasma electrons and is often described by a Maxwellian distribution. In colliding beams experiments with electrons and ions, f is usually a distribution centered at an average relative velocity v_{rel} of the colliding particles.

$$\alpha(v_{rel}) = \int \sigma(v) v f(v_{rel}, \mathbf{v}) \mathrm{d}^3 v \tag{9}$$

Equation (8) can now be written in the form

$$R = \alpha n_e \ell_{eff} I_i / (q e v_i \gamma^2) \tag{10}$$

In (10) an additional factor $\gamma^2 = [1 - (v_i/c^2)]^{-1}$ has been introduced to account for the relativistic transformation between the center-of-mass and the laboratory frames. In the present experiment this factor has an effect of less than 2 %.

The factor α occuring above is usually only then called a "rate coefficient" in the literature, when $f(v)$ is an isotropic Maxwellian distribution characterized by a temperature T. In a merged beams experiment α has a slightly different meaning. Its definition is given by (9) . Here, v_{rel} and f still have to be specified in order to provide an unambigous physical quantity α accessible to experimental evaluation.

For the energy-analyzed ion beam in the present experiment, the distribution function f is dominated by the electron velocity distribution because of the large mass difference between electrons and ions. With respect to the kinematics in the experiment and the axial symmetry of the electron and ion beams, two velocity coordinates are necessary to describe this distribution: $v_{\|}$ the velocity component in electron beam direction and $v_{\perp}$ the velocity component perpendicular to the electron beam direction. The energy (or velocity) spreads are therefore characterized by two corresponding temperatures $T_{\|}$ for the longitudinal and $T_{\perp}$ for the transverse direction. In the accelerated electron beam these temperatures are quite different with $T_{\|} \ll T_{\perp}$, so that $f(v)$ is highly anisotropic and is therefore often called a "flattened" electron velocity distribution. Its mathematical form is given by

$$f(v_{rel}, \mathbf{v}) = \frac{m_e}{2\pi k T_{\perp}} \exp\left(-\frac{m_e v_{\perp}^2}{2kT_{\perp}}\right) \times \sqrt{\frac{m_e}{2\pi k T_{\|}}} \exp\left(-\frac{m_e (v_{\|} - v_{rel})^2}{2kT_{\|}}\right), \tag{11}$$

where k denotes Boltzmann's constant. The quantity v_{rel} in this formula is the average longitudinal center-of-mass velocity

$$v_{rel} = |v_{e,\|} - v_{i,\|}| / (1 + |v_{i,\|} v_{e,\|}| / c^2), \tag{12}$$

where $v_{e,\|}$ and $v_{i,\|}$ are the longitudinal velocity components of the electron and ion beams, respectively. They are determined from

$$\begin{aligned} v_{e,\|} &= c\sqrt{1 - [1 + E_e/(m_e c^2)]^{-2}} \\ v_{i,\|} &= c\sqrt{1 - [1 + E_i/(m_i c^2)]^{-2}}. \end{aligned} \tag{13}$$

The energies E_e and E_i are determined by acceleration potentials and do not include additional kinetic energy (with randomly oriented velocity vectors) due to finite beam temperatures. Therefore, the relative velocity v_{rel} as defined by (12) can be different from the velocity v_{cm} in the electron-ion center-of-mass frame. This is particularly true for low energies, where E_{cm} comes close to $kT_{\perp,\|}$. At high center-of-mass energies E_{cm}, clearly $v_{rel} = v_{cm}$. At low E_{cm}, v_{rel} can be much less than v_{cm}. Since it is the only one of the two quantities directly accessible to a measurement, experimental data are usually displayed as a function of the relative energy E_{rel}. Therefore cross section or rate data in the literature are displayed for energies E_{rel} reaching as far down as to 10^{-3} eV, although the energy spread in the center-of-mass frame is 10^{-1} eV or more (which becomes visible e.g. by the energy spread in the measured resonance peaks). Because of the lack of an alternative we also display in the present paper rates and cross sections as a function of E_{rel}. The energies are calculated by using the correct relativistic transformation according to (7).

By the experiments, normalized rates α are determined from

$$\alpha(E_{rel}) = \frac{R\gamma^2 v_i q e}{I_i \ell_{eff} n_e \varepsilon} \tag{14}$$

The number of recombinations per unit time R is determined from the counting rate of the position sensitive detector. These rates were so low (well below $10^4\ \mathrm{s}^{-1}$ instantaneous), that the dead time losses were very small. Necessary corrections were made on the basis of the information from two counting channels with different dead time constants (see section on experimental procedures). The detection efficiency ε of the detector has been already discussed above. A value $\varepsilon = 0.95 \pm 0.05$ is used in the determination of normalized rates and cross sections. The relativistic Lorentz factor γ is within 2 % of 1.00 and its uncertainty can be neglected. It is determined from the ion energy E_i as measured by a time-of-flight technique which results in a maximum relative uncertainty $\Delta E_i / E_i$ of 0.1 %. This same measurement also yields v_i with half the relative uncertainty of E_i. The total electrical ion current I_i is measured with a relative uncertainty of 5 %. The application of (14) requires, however, that the ion beam is completely contained inside the electron beam. Therefore, an additional uncertainty of I_i (or more precisely: the average number of ions instantaneously present inside the electron beam) has to be considered. This uncertainty can be obtained from ion beam losses to the diagnostic slits in the electron target when these slits are set to 3 mm diameter, i.e. when they just touch the volume occupied by the electron beam. Of course, the electron beam has to be switched off for such a measurement as described above. The currents measured on the different slit jaws were at most 20 % of the current collected in the final Faraday cup. Considering that there is no suppression of secondary electrons emitted from the slit surfaces, the real current loss is probably even less. Current lost in this diagnostic part of the experiment means current that does not go through the electron beam even when the slits are opened again and hence, a reduced number of ions in the interaction volume or

a reduced ion current should be used in (14). Using the currents lost in a measurement as described above, we corrected the current I_i and allow an additional relative uncertainty of 20 %.

The effective target length is determined from the distance of the two sets of slits which define the limits of the interaction region. Outside this region the electric potential is zero without the electron beam and only altered by the electron space charge. Hence, the electron energy outside the interaction region is different from that in the interaction volume and stays constant during a scan of U_{int}. Thus, it can at most contribute to the energy-independent background of the observed electron-ion recombination. Moreover, the electron beam is displaced from the axis in that region, the merging and separating sections of the electron target, and the finite angles with respect to the ion beam quickly lead to very high collision energies where no strong resonances in the recombination are expected. So the uncertainty of ℓ_{eff} = 42.5 cm is only due to the potential distribution around the slits due to their finite aperture. A relative uncertainty of 7 % is estimated.

Finally, the electron density follows directly from the measured electron current I_e with $n_e = I_e/(ev_e\pi r^2)$, where r = 1.5 mm is the radius of the electron beam. The uncertainty of the electron current measurement is 7 %. Compared to that, the uncertainties of v_e and r are negligible. Hence, also the uncertainty of n_e is 7 %. The above uncertainties can be assumed to be independent of each other. The overall most probable systematic uncertainty of the measured rate α is therefore determined from the square root of the sum of all squared relative uncertainties of the quantities entering (14). This uncertainty is ±24 %. In the figures, displayed in this paper, only statistical uncertainties are shown. For obtaining the total probable uncertainty, the statistical uncertainties have to be included in the quadrature sum of all possible errors.

Apart from the uncertainty of the measured rates α, the possible error of the collision energy is also very important. The main source of uncertainty of E_{rel} is the degree of electron space charge compensation which can vary when U_{int} is scanned. It was mentioned in the section about the experimental procedures that the space charge of the electron beam causes an overall potential depression of several hundred Volts. This is partly offset by slow positive ions trapped inside the electron beam. As long as this compensation is constant, there is only a shift in the electron energy with respect to the case of an uncompensated electron beam. This requires that the pure space charge contribution to the total potential of the interaction region does not change when the voltage set to the strip electrodes is varied. The shift can be easily measured by observing the appearance of the maximum in the recombination rate which occurs at v_{rel} = 0 (see Fig. 6). Thus, the experiment can be used to calibrate the measured U_{int} (for known cathode potential U_C) to the real electron energy E_{rel}. There is an uncertainty, however, because of possible variations of the space charge compensation. In the experiments reported in this paper variations of the degree of space charge compensation were observed

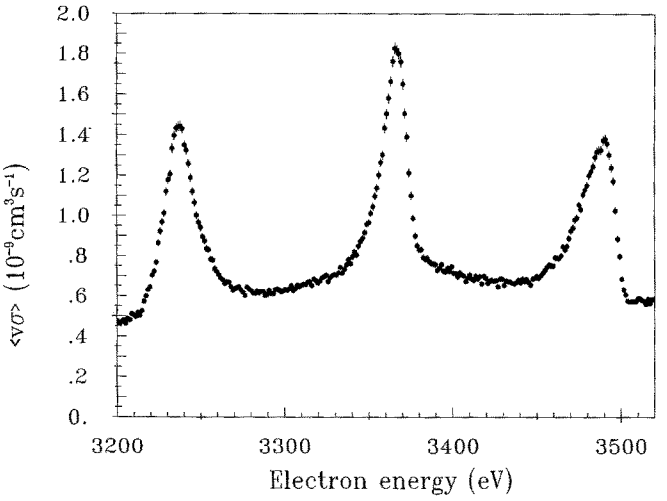

Fig. 6. Experimental rate for recombination of 5.96 MeV/u Ar^{15+} ions and free electrons as a function of the apparent electron laboratory energy. At about 3365 eV the parallel velocity components of electrons and ions are matched and the RR rate shows its maximum. The true electron energy is slightly less because of the negative space charge of the electron beam. DR resonances are marked by the intermediate states populated during the collision. Background is not subtracted

leading to laboratory energy shifts of a few eV. This results in uncertainties of resonance energies of only about 0.2 eV at E_{rel} = 1 eV, of 2.5 eV at E_{rel} = 35 eV and up to 14 eV at E_{rel} = 525 eV.

7. Experimental results

Figure 6 displays a normalized spectrum of the experimental recombination rate (obtained by the detection of recombined Ar^{14+} ions in the present setup) versus the apparent laboratory energy $E_{app} = e\,(U_{int} - U_C)$ of the electron beam. The parent ion beam consisted of 5.96 MeV/u Ar^{15+} ions. Background, arising mostly from collisions of the fast ions with residual gas atoms or molecules and also from slit scattering, is not subtracted. In the present example this background leads to an apparent uniform rate of 3 to $4 \cdot 10^{-9}$ cm^3s^{-1}. At an apparent electron energy of E_{app} = 3365 eV there is a peak which one can attribute to RR at v_{rel} = 0. Since the ion energy is known, one can calculate an electron laboratory energy of 3270 eV for the peak. The difference of the two numbers is due to the space charge of the electron beam and the trapped slow ions. The two peaks at 3240 eV and 3490 eV correspond to $E_{rel} \approx 1$ eV and are due to the DR leading to an intermediate configuration $1s^2 2p_{1/2} 10\ell$. The spectrum is roughly symmetrical about the matching energy as suggested by the kinematics given in Fig. 5. The left peak is due to a situation where the ions are faster than the electrons, the right peak occurs when the ions are slower than the electrons. In both cases the relative velocity is the same and hence also the collision energy. Therefore the same resonance is seen at two different settings of U_{int}.

It is known from theory that the cross section for RR [24, 25] rapidly drops with increasing relative energy E_{cm} between the electrons and the ions. Hence, the background

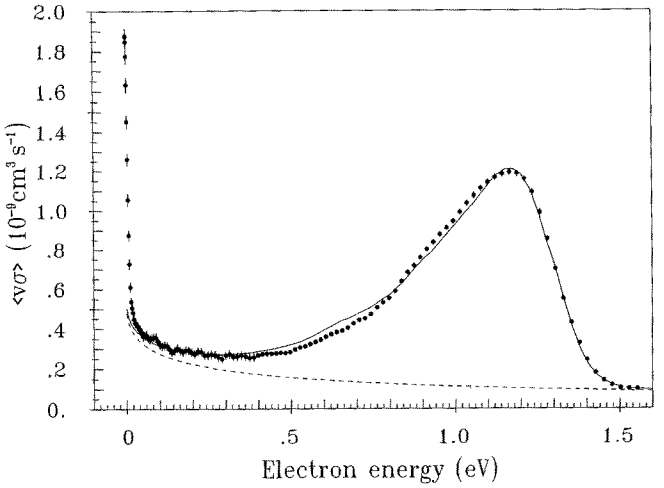

Fig. 7. Recombination rates for Ar^{15+} ions and electrons versus the relative energy E_{rel} (see text). The experimental data are displayed with their statistical error bars. The dashed curve represents the present RR calculation. The solid line is the sum of these RR rates and theoretical DR rates with slightly shifted resonance energies. The electron beam temperatures correspond to $kT_{\|} = 0.0024$ eV and $kT_{\perp} = 0.26$ eV

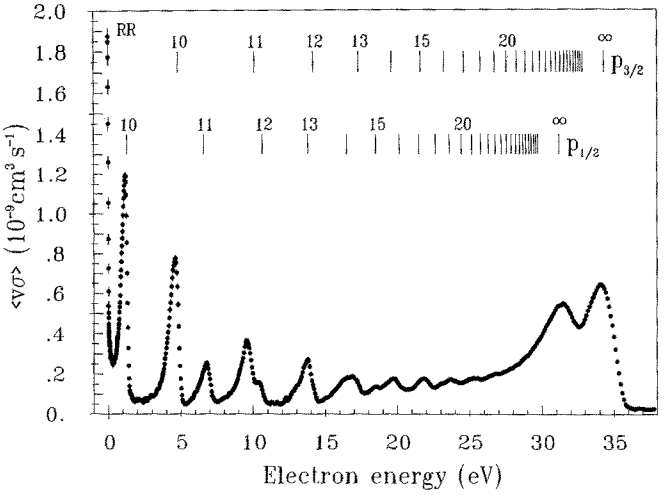

Fig. 8. Recombination rates for Ar^{15+} ions and electrons observed for relative electron energies E_{rel} up to about 38 eV. The DR resonances involve $\Delta n = 0$ transitions of the $2s$ core electron. The experimental data are displayed with their statistical error bars. The energies of Rydberg states with configurations $1s^2 2p_{1/2} n\ell$ and $1s^2 2p_{3/2} n\ell$, populated during the recombination process, are indicated by vertical lines

observed in addition to the DR resonances becomes quite flat already for E_{rel} greater than or about equal to 5 eV. Therefore, subtraction of the energy-independent background is straightforward. The remaining normalized rate is shown in Fig. 7 as a function of E_{rel} for the raw data displayed in Fig. 6. Only the low-energy branch of the data was used, since it provides better energy resolution. By the transformation of the measured spectrum into the system of relative energy the peak at $E_{rel} = 0$ eV has become remarkably narrow. It is much more pronounced than expected on the basis of the available theory for RR. An additional mechanism (e.g. collisional radiative recombination) has to be invoked in order to explain the enhanced recombination rate at the lowest relative energies [26]. This part of the measurement is not well understood yet and will have to be studied in more detail. In the present paper we exclude the discussion of recombination processes other than DR. Only for the data presented in Fig. 7 we show an estimate of the rate of RR of Ar^{15+} in order to discuss the background of DR resonances.

The peak at about 1 eV in the measurement displayed in Fig. 7 is asymmetric with a relatively sharp cutoff towards higher relative energies. This phenomenon has been discussed previously [6]. It is a consequence of the "flattened" electron velocity distribution in the electron beam and reflects the difference of $T_{\perp}$ and $T_{\|}$. These two quantities may in return be determined by a fit of convoluted rates (calculated according to (9) and (11) to the measured data. In the present example, calculated energy-binned cross sections (see Sect. 8. of this paper) were convoluted with the distribution function (11) and as a best fit the following parameters were found: $kT_{\perp} = 0.26$ eV and $kT_{\|} = 0.0024$ eV. The solid line in Fig. 7 is the sum of our calculation of the rate for radiative recombination and of the rate for DR into the particular intermediate configuration $1s^2 2p_{1/2} 10\ell$. Only the theoretical energy of the resonance was slightly shifted (by 0.14 eV) to better match the experimental result. The temperatures obtained from this analysis are in good agreement with the design values of the electron target. Considering the fact that the density of electrons is a factor of more than 100 above the density in similar devices, it is very remarkable that a radial temperature increase of only a factor 2 to 3 can be realized. This is important for the following presentation of results.

The experimental spectrum of the measured rates for electron-ion recombination in the energy range of the $\Delta n = 0$ core transitions is shown in Fig. 8. As expected, one can see resonances from two separate Rydberg series of intermediate states with configurations $1s^2 2p_{1/2} n\ell$ and $1s^2 2p_{3/2} n\ell$. The expected energies for the different Rydberg states of each series are indicated by vertical markers at the top of the figure. Clearly, structure in the spectrum is visible for Rydberg quantum numbers up to about 20. At the two series limits, resonances pile up to produce two well separated peaks showing the resolution of the $1s^2 2p_{1/2}$ and $1s^2 2p_{3/2}$ fine-structure splitting. The peak denoted RR is only partly due to RR. An additional contribution from collisional radiative recombination has been suggested [26], which can significantly contribute only at very low relative energies and at high electron densities. This phenomenon is being treated in a separate investigation and will not be discussed here in more detail.

Figure 9 displays our experimental results for DR of Ar^{15+} ions with $\Delta n = 1$ core transitions. This time, averaged cross sections $<\sigma>$ are displayed since the energies are already so high compared to the energy spreads that $<\sigma>$ can be obtained from α / v_{rel} (see (9-14)). All intermediate configurations $1s^2 3\ell n\ell'$ with $n \geq 3$ are included in the investigated energy range. Rydberg states with quantum numbers up to $n = 9$ are resolved. For the lower n numbers even some fine-structure splitting becomes visible. This is particularly true for the $1s^2 3\ell 3\ell'$ configuration where four

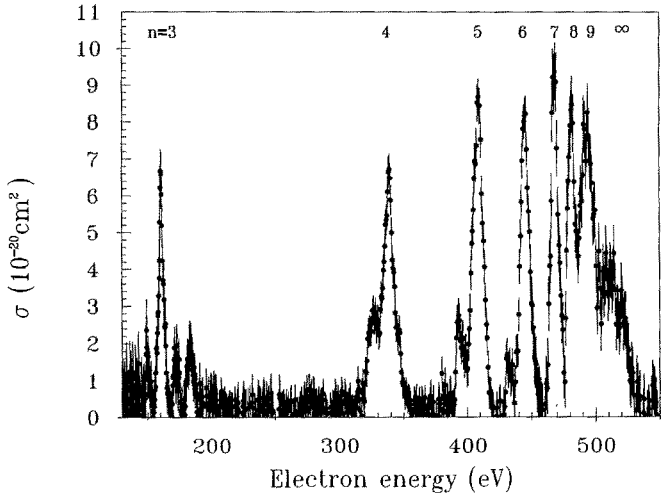

Fig. 9. Energy averaged cross sections $<\sigma>=<v_{rel}\sigma>/v_{rel}$ for DR of Ar^{15+} ions involving Δn = 1 core transitions. Intermediate states with configurations $1s^2 3\ell n\ell'$ are marked by the corresponding principal quantum numbers n. The experimental data are shown together with their statistical uncertainties

sublevels can be distinguished (see also Fig. 12).

For the understanding of the present experimental results it is necessary to discuss the influence of electric fields on the measured rates. Electric fields are present during the recombination process inside the electron beam. Such fields may be due to the space charge potential distribution inside the target or due to non-zero field components of the magnetic solenoid field with respect to the ion beam. Already a divergence of the ion beam of 1 mrad can produce an apparent electric field $|\mathbf{v_i} \times \mathbf{B}| \approx 200\,\mathrm{V\,cm^{-1}}$ in the present experiment. Also the space charge of the electrons can result in electric fields of the order of hundreds of $\mathrm{V\,cm^{-1}}$. Beyond the interaction region, the ions have to pass through the transverse magnetic field component of the electron target which was up to about 0.1 T. The resulting motional electric field has a strength of roughly $34\,\mathrm{kV\,cm^{-1}}$. Electric fields with different directions are then felt by the ions when they pass through the steering magnets and the magnetic quadrupole lenses, however, the maximum field is envisaged in the analyzing magnet. A good estimate of the field strength experienced in the analyzing magnet by an ion with charge state q, mass number A, and specific energy E (in MeV/u) is $F = 7550 A\,E/q\,\mathrm{V\,cm^{-1}}$. Here, the bending radius ρ = 2730 mm of the magnet has been used. For the present example this results in a field strength of $120\,\mathrm{kV\,cm^{-1}}$.

Electric fields have a number of effects on the measurements presented here. For high Rydberg states the rate of DR itself can be enhanced when electric fields are present (see also the section on theory). Lifetimes of states change with the presence of fields and depending on the slew rates of the fields seen by the ions there may be a rearrangement of states when an ion "collides" with an electric field. Last not least field ionization will occur in an electric field F stripping off Rydberg electrons with quantum numbers $n > n_{max}$. In reality, there is no sharp cutoff in the Rydberg state distribution [27], however, the often used formula [28]

$$n_{max} = \left(\frac{6.8 \cdot 10^8 q^3\,\mathrm{V\,cm^{-1}}}{F}\right)^{1/4} \quad (15)$$

gives a reasonable estimate of the range of principal quantum numbers up to which an ion state can survive a given electric field F. For the present investigation $n_{max} \approx 64$. In the analyzing magnet, all Ar^{14+} ions in Rydberg states with $n > 64$ are field ionized and do not reach the detector. (As mentioned above, there is a range of n-values rather than a sharp cutoff, adding even more complication to the present discussion.) Between the electron target (where $n_{max} \approx 90$) and the analyzing magnet, however, some of the ions with $90 > n > 64$ can already undergo transitions to states with $n \leq 64$ and will thus be detected as Ar^{14+} ions and contribute to the signal. The experiment does not directly provide numbers for the effects discussed above. In connection with theory, however, the role of Rydberg states beyond n_{max} can be discussed. In some cases, a contribution of high Rydberg states can be ruled out anyway and then the true cutoff does not matter (as is the case in the present investigation). A systematic measurement of recombination rates, in which the ion energy is changed over a considerable range, would possibly provide some insight into the problem involved with the high Rydberg states. In the present experimental arrangement the motional electric field is directly proportional to the specific ion energy and hence, a certain range of n_{max} might be studied by variation of the ion energy and its influence on the experimental rate might then be observed.

8. Theory

In the isolated-resonance approximation, the energy-averaged DR cross section for a given initial level i through an intermediate level j is given by [29]

$$\bar{\sigma}(i \to j) = \frac{2\pi^2}{\Delta\epsilon\, k^2}\frac{g_j}{2g_i}\frac{A_a(i \to j)\sum_f A_r(j \to f)}{\sum_m A_a(j \to m) + \sum_f A_r(j \to f)} \quad (16)$$

The above equation is in atomic units and $\Delta\epsilon$ is an energy bin width larger than the largest resonance width, k is the linear momentum of the continuum electron, g_j is the statistical weight of the N-electron target level. First-order many-body perturbation theory is used to evaluate both the radiative, A_r, and autoionization, A_a, rates for the many intermediate levels j in the energy range of interest. To evaluate (16) for the Δn = 0 transitions in Ar^{15+}, we made use of the previously written computer code DRFEUD [30] which calculates intermediate-coupled single-configuration DR cross sections for low n explicitly and for high n by extrapolating matrix elements of the dipole radiative and electron-electron Coulomb interactions. In the presence of an external electric field, the doubly excited levels for each n are constructed from the matrix diagonalization of a Hamiltonian which includes Stark ℓ-mixing effects. These field-mixed levels are

then used to calculate radiative and autoionizing rates which, in turn, provide a field-dependent DR cross section. We ignore mixing between different n states, and the effects that the electric field may have on the continuum electron.

To evaluate (16) for the $\Delta n = 1$ transitions in Ar^{15+}, we made use of the previously written computer code AUTOSTRUCTURE [31, 32] which calculates LS-coupled or intermediate-coupled multi-configuration DR cross sections for low n explicitly and for high n by extrapolating radial wavefunctions using quantum-defect theory. External electric field effects are not included in the AUTOSTRUCTURE code.

$2s \rightarrow 2p$ core excitations

For DR in Ar^{15+} involving $\Delta n = 0$ transtions we consider the following reaction pathways:

$$\begin{array}{l} e + (1s^2 2s) \rightleftharpoons \\ (1s^2 2pn\ell) \rightarrow \left\{ \begin{array}{l} (1s^2 2sn\ell) \\ (1s^2 2pn'\ell') \end{array} \right\} + h\nu, \; n \geq 10. \\ \quad \downarrow \\ (1s^2 2p) + e \end{array} \tag{17}$$

The Auger decay channel $(1s^2 2p + e)$ depends on the $2p(j = 1/2)$ to $2p(j = 3/2)$ core splitting and is available only for relatively high n values. The calculation includes final states with $n \leq n_{max} = 64$, which is determined to be the maximum value which survives field ionization by the charge-state analyzer. We find that results are insensitive to the precise value of the cut-off used.

$2s \rightarrow 3\ell$ core excitations

For DR in Ar^{15+} involving $\Delta n = 1$ transitions we consider the following reaction pathways:

$$\begin{array}{l} e + (1s^2 2s) \rightleftharpoons \\ (1s^2 3pn\ell) \rightarrow \left\{ \begin{array}{l} (1s^2 2\ell' 3p) \\ (1s^2 2sn\ell) \end{array} \right\} + h\nu, \; n \geq 3, \\ \quad \downarrow \\ (1s^2 2p) + e \end{array} \tag{18}$$

and

$$\begin{array}{l} e + (1s^2 2s) \rightleftharpoons \\ \left\{ \begin{array}{l} (1s^2 3sn\ell) \\ (1s^2 3dn\ell) \end{array} \right\} \rightarrow \left\{ \begin{array}{l} (1s^2 2\ell' 3s) \\ (1s^2 2\ell' 3d) \end{array} \right\} + h\nu, \; n \geq 3, \\ \quad \downarrow \quad \downarrow \\ \quad (1s^2 2p) + e \\ \downarrow \\ (1s^2 2pn\ell) + h\nu \rightarrow \left\{ \begin{array}{l} (1s^2 2sn\ell) \\ (1s^2 2pn'\ell') \end{array} \right\} + h\nu + h\nu', \quad \begin{array}{l} n \geq 3, \\ n' \leq 10 \end{array} \\ \downarrow \\ (1s^2 2s) + e \quad n > 10 \end{array} \tag{19}$$

The reaction pathway of (18) corresponds to the normal DR process, that is of dielectronic capture followed by radiative stabilization. However, the reaction pathway of (19) includes a pathway to recombination that requires radiative cascade. This requires that (16) for the DR cross section be multiplied by an additional fluorescence yield $A_r/(A_r + A_a)$. Configuration mixing effects within the $1s^2 3\ell n\ell$ complex were included for $n = 3$ and $n = 4$, but were found to be negligible for higher n.

9. Comparison of theory and experiment

Theoretical cross section data can only be compared to the experimental results directly, when they are convoluted with the experimental energy spread. The convolution has to be carried out according to (9). If the variance of $f(v_{rel}, \mathbf{v})$ is small compared to v_{rel}, it is reasonable to deduce from the measured rate α the energy-averaged experimental cross section $<\sigma> = \alpha/v_{rel}$. This has been applied to the $\Delta n = 1$ dielectronic resonances displayed in Fig. 9, while the condition for extracting an experimental cross section were not fulfilled in the energy range of the $\Delta n = 0$ resonances. Therefore, these data are the experimental rates α which have to be compared with the theoretical data convoluted according to (9). The temperatures $T_\perp$ and $T_\parallel$ are chosen to match the experimental line shapes. Typical numbers have been discussed in the context of Fig. 7.

$2s \rightarrow 2p$ core excitations

Figure 10 shows a comparison of the experimental data on $2s \rightarrow 2p$ core excitations with theory. Different from Fig. 8, the contribution of RR (and possibly collisional RR) has been subtracted by using an extrapolation of the measured low-energy rates and the known energy dependence of the cross section for RR. For the convolution according to (9), the following parameters have been used: $kT_\perp = 0.33$ eV and $kT_\parallel = 3.5 \cdot 10^{-3}$ eV.

Overall, there is good agreement between theory and experiment for the $1s^2 2pn\ell$ resonances from 0 to 20 eV incident energy. At higher energies the DR cross sections calculated for zero electric field (E_c) in the collision region are about a factor of 3 below the experimental measurements (see dashed line in Fig. 10), showing that electric fields in the experiment strongly enhance the Rydberg series limit peaks at 31 eV ($j = 1/2$) and 34 eV ($j = 3/2$). With the inclusion of an electric field $E_c = 100$ V/cm, the calculations (solid line in Fig.10) are in reasonable agreement with experiment for the $j = 1/2$ peak, but the $j = 3/2$ peak is above the experiment.

The peak positions do not always line up perfectly in theory and experiment. The most probable reason for this is in the uncertainty of the experimental energy axis due to varying degrees of space charge compensation during the scan

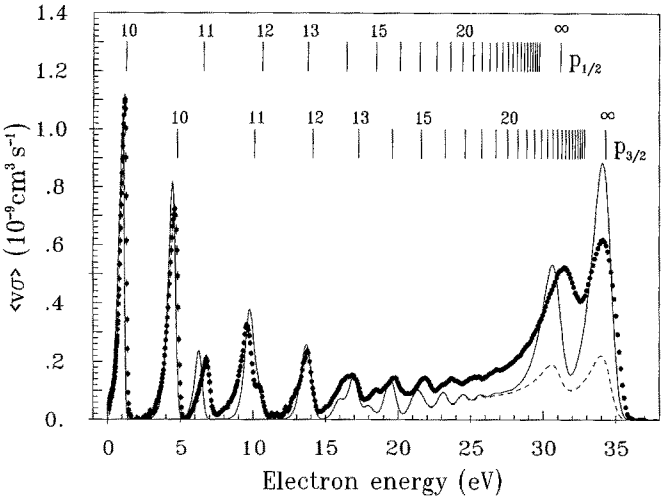

Fig. 10. Dielectronic recombination rates for Ar^{15+} ions and electrons involving $\Delta n = 0$ transitions of the $2s$ core electron. The experimental data points were obtained by subtracting a calculated RR rate from the measured rates $\alpha = < v_{rel}\sigma >$. The experimental data are displayed with their statistical error bars. The energies of Rydberg states with configurations $1s^2 2p_{1/2} n\ell$ and $1s^2 2p_{3/2} n\ell$, populated during the recombination process, are indicated by vertical lines. An electric field $E_c = 100$ V cm^{-1} in the interaction region of electrons and ions has been invoked to reproduce the magnitude of the peaks at the series limits of the $2pn\ell$ resonances (*solid line*). In the zero-field limit a much reduced rate has been calculated for the high Rydberg states (*dashed-line*)

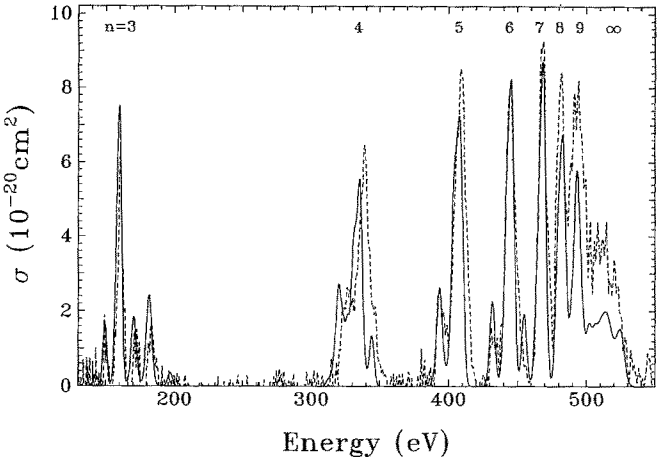

Fig. 11. Comparison of theory and experiment on energy averaged cross sections $<\sigma>=<v_{rel}\sigma>/v_{rel}$ for DR of Ar^{15+} ions involving $\Delta n = 1$ core transitions. Intermediate states with configurations $1s^2 3\ell n\ell'$ are marked by the corresponding principal quantum numbers n. The experimental data are shown as a *dashed line* connecting the measured cross sections. For better visibility of differences statistical uncertainties are not given here. The theoretical curve, represented by a *solid line*, includes partial cascade (see text)

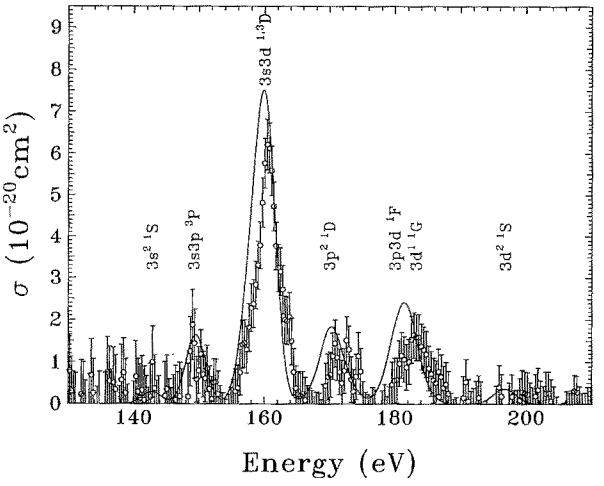

Fig. 12. Comparison of theory (*solid line*) and experiment (*data points with statistical-error bars*) for energy averaged cross sections $<\sigma>= <v_{rel}\sigma>/v_{rel}$ for DR of Ar^{15+} ions involving a $\Delta n = 1$ core transition to intermediate states with configurations $1s^2 3\ell 3\ell'$. Term assignments to the peaks are given

measurements. Another discrepancy between theory and experiment occurs between about 15 eV and 28 eV. The experimental rate is roughly a factor two bigger than the theoretical one. A similar discrepancy has been observed before by Andersen et al. for lithium-like ions [6, 7]. There is no explanation for this observation so far.

$2s \rightarrow 3\ell$ core excitations

Figure 11 shows a comparison of the experimental data on $2s \rightarrow 3\ell$ core excitations with theory. At the high energies E_{rel} under discussion in this context, $T_\perp$ of the electron beam does not play a role. The energy spread is determined by the longitudinal electron beam temperature and the resonance peaks can be described by Gaussians with $FWHM = 4\,(\ln(2)\,E_{rel}\,kT_\parallel)^{1/2}$. The experimental widths are best reproduced by $kT_\parallel = 0.0075$ eV for the measurement of the $3\ell 3\ell'$ resonances and $kT_\parallel = 0.0035$ eV else. The differences are explained by the fact that the data were taken in separate scan measurements with slightly different qualities of the electron beam. Overall, there is good agreement between theory and experiment for $n < 10$. More detailed views are presented in Figs. 12 and 13. Figure 12 provides an enlarged plot of the data from the group of intermediate $1s^2 3\ell 3\ell'$ states. Term assignments to the resonances resolved in this experiment are given. The experimental cross sections found for the $1s^2 3\ell 3\ell'$ resonances agree with theory within less than 10 %. Slight shifts of peak energies are observed between theory and experiment. This is also true for the resonances at higher energies. Again, these discrepancies are attributed to the uncertainty in the experimental energy determination rather than to the theory. The experimental uncertainty in energies is due to small space charge variations during the scan measurements.

Although there is a substantial drop in both the theoretical and experimental cross sections for $n \geq 10$, theory underestimates the cross section by nearly a factor of two compared to experiment (see Fig. 13). The substantial drop in cross section observed for $n \geq 10$ is due to the fact that the dominant DR process is $2s + e \rightarrow 3dn\ell \rightarrow 2pnl + h\nu$, for which $2pn\ell \rightarrow 2s + e$ is energetically allowed for $n \geq 10$. Theoretically, we find that there is little cascading, just compare the no-cascade and partial cascade curves (fluorescence yields equal to 0 and $A_r/(A_r + A_a)$, respectively) in Fig. 13. The full cascade curve (yield = 1) shows that there is a large reservoir of states that could contribute to the recombination process, but in our current theoretical description in fact au-

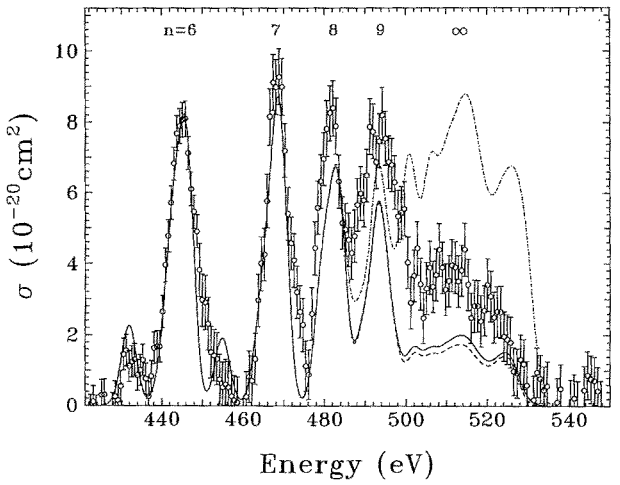

Fig. 13. Comparison of theory and experiment on energy averaged cross sections $\langle\sigma\rangle = \langle v_{rel}\sigma\rangle / v_{rel}$ for DR of Ar^{15+} ions involving $\Delta n = 1$ core transitions to intermediate states with configuration $1s^2 3\ell n\ell'$ where $n \geq 6$. The experimental data are shown together with their statistical uncertainties. The theoretical curve, represented by a *solid line*, includes partial cascade (see text). Also shown are theoretical cross sections obtained under the assumptions of no cascade (*dashed curve*) and full cascade (*dot-dashed curve*). The latter shows the reservoir of intermediate states which could contribute to DR provided they would all stabilize via photoemission

toionize, i.e. they contribute to resonant-excitation instead. The one obvious omission from our calculations is the effect of electric fields which would increase the population of the high-ℓ states due to dielectronic capture. This would merely redistribute the DR cross section in the absence of cascade since $A_a(3 \rightarrow 2) \ll A_r(3 \rightarrow 2)$ for the field-affected high-n. In the presence of cascade, field-mixing could increase the DR cross section since the high-ℓ fluorescence yields are larger than the low-ℓ yields, at least in the zero-field case. The field-redistributed autoionization rates also lead to a reduction in the high-ℓ fluorescence yields. It would require an explicit intermediate coupling field-dependent cascade calculation to determine the size of any field-enhancement in this case, but this is beyond the scope of the current computer codes.

10. Conclusions

We have described with some detail a new experimental facility, set up at the UNILAC of GSI in Darmstadt for the purpose of recombination studies on highly charged ions and free electrons. The electron target designed for this experiment can provide an electron density nearly a factor of 1000 higher than densities reached in similar devices, including the electron cooler devices of ion storage rings. Nevertheless, the radial electron temperature is less than 0.5 eV/k and thus the present electron target provides features which are not available at any other laboratory worldwide. In particular, the target allows to study density effects on recombination at very low relative energy of electrons and ions. A research program aimed at this topic is underway and has provided first exciting data.

In the present paper, DR of lithium-like Ar^{15+} ions is studied both experimentally and theoretically. The measurements are used to characterize the properties of the present merged beams arrangement and to check the design values of the electron target. At the same time, new data on both $\Delta n = 0$ and $\Delta n = 1$ core transitions are obtained and compared to theory. The present data provide a test case for an intermediate atomic number ($Z = 18$) additional to the previous measurements carried out at Aarhus with lithium-like ions up to Si^{11+} (limited to $\Delta n = 0$) and at the TSR in Heidelberg with lithium-like Cu^{26+}. At the series limit of $1s^2 3\ell n\ell'$ states, the present experiment with its high density electron target and the resulting high luminosity provides a level of statistics which allow the determination of a discrepancy between theory and experiment at energies where cascading from the intermediate highly excited states populated by DR begins. This discrepancy has not yet been explained. The comparison of the present experiment with theory also shows features for the $\Delta n = 0$ core transitions which are not explained. These again involve the contributions of intermediate states with higher Rydberg quantum numbers.

We are grateful to many colleagues, students and members of the technical staff for their interest, their support and their active contributions to the present project. Their names, listed in alphabetical order, are: E. M. Bernstein, F. Bosch, D. Brill, N. Djurić, H. Emig, L. Empacher, W. Enders, I. Hofmann, B. Jelenković, J. Klabunde, K.-D. Leible, I. Müller, R. Ortlieb, K. Poppensieker, U. Pröbstel, H. Schulte, P. Spädtke, M. Terasawa, K. Valadkhani, B. Wolf. A part of the present work was carried out at the Institut für Kernphysik of the University of Giessen. We thank E. Salzborn for his interest and support. We are pleased to acknowledge support from Bundesministerium für Forschung und Technologie, Bonn-Bad Godesberg (contract numbers: 06 OF 656, 06 OF 304, 06 GI 658/II, 06 GI 308). The Giessen-Stuttgart group also acknowledges financial support through the university-collaboration program of GSI, Darmstadt (contract numbers: GI MU C, GI Mül A).

References

1. Summers, H. P., Dickson, W. J.: In: Recombination of Atomic Ions, Graham, W. G., Fritsch, W., Hahn, Y., Tanis, J. A. (eds.) NATO ASI Series B: Physics Vol. 296, pp. 31-48. New York: Plenum 1992
2. Dunn, G. H.: In: Recombination of Atomic Ions, Graham, W. G., Fritsch, W., Hahn, Y., Tanis, J. A. (eds.) NATO ASI Series B: Physics Vol. 296, pp. 115-131. New York: Plenum 1992
3. Dittner, P. F., Datz, S.: In: Recombination of Atomic Ions, Graham, W. G., Fritsch, W., Hahn, Y., Tanis, J. A. (eds.) NATO ASI Series B: Physics Vol. 296, pp. 133-141. New York: Plenum 1992
4. Graham, W. G., Fritsch, W., Hahn, Y., Tanis, J. A. (eds.): Recombination of Atomic Ions, NATO ASI Series B: Physics Vol. 296. New York: Plenum 1992
5. Dittner, P. F., Datz, S., Krause, H. F., Miller, P. D., Pepmiller, P. L., Bottcher, C., Fou, C. M., Griffin, D. C., Pindzola, M. S.: Phys. Rev. **A 36**, 33 (1987)
6. Andersen, L. H., Bolko, J.: Phys. Rev. **A 41**, 1293 (1990)
7. Andersen, L. H., Pan, G.-Y., Schmidt, H. T., Pindzola, M. S., Badnell, N. R.: Phys. Rev. **A 45**, 6332 (1992)
8. Kilgus, G., Habs, D., Schwalm, D., Wolf, A., Badnell, N. R., Müller, A.: Phys. Rev. **A 46**, 5730 (1992)
9. Spies, W., Müller, A., Linkemann, J., Frank, A., Wagner, M., Kozhuharov, C., Franzke, B., Beckert, K., Bosch, F., Eickhoff, H., Jung, M., Klepper, O., Koenig, W., Mokler, P. H., Moshammer, R., Nolden, F., Schaaf, U., Spädtke, P., Steck, M., Zimmerer, P., Grün, N., Scheid, W., Pindzola, M. S., Badnell, N. R.: Phys. Rev. Lett. **69**, 2768 (1992)

10. Spies, W., Müller, A., Kozhuharov, C., Linkemann, J., Frank, A., Franzke, B., Wagner, M., Beckert, K., Bosch, F., Eickhoff, H., Jung, M., Klepper, O., Koenig, W., Mokler, P. H., Moshammer, R., Nolden, F., Schaaf, U., Spädtke, P., Steck, M., Zimmerer, P., Grün, N., Scheid, W., Pindzola, M. S., Badnell, N. R.: Proceedings of the XVIIIth International Conference on the Physics of Electronic and Atomic Collisions, Aarhus, Denmark, 21.07. - 27.07.1993, Abstracts of Contributed Papers, p. 375
11. Uwira, O., Spies, W., Kozhuharov, C., Müller, A., Linkemann, J., Franzke, B., Beckert, K., Bosch, F., Eickhoff, H., Jung, M., Klepper, O., Mokler, P. H., Moshammer, R., Nolden, F., Schaaf, U., Spädtke, P., Steck, M.: Proceedings of the XVIIIth International Conference on the Physics of Electronic and Atomic Collisions, Aarhus, Denmark, 21.07. - 27.07.1993, Abstracts of Contributed Papers, p. 377
12. Müller, A., Schennach, S., Wagner, M., Haselbauer, J., Uwira, O., Spies, W., Jennewein, E., Becker, R., Kleinod, M., Pröbstel, U., Angert, N., Klabunde, J., Mokler, P. H., Spädtke, P., Wolf, B.: Phys. Scri. **T37**, 62 (1991)
13. Schennach, S., Müller, A., Wagner, M., Haselbauer, J., Uwira, O., Spies, W., Jennewein, E., Becker, R., Kleinod, M., Pröbstel, U., Angert, N., Klabunde, J., Mokler, P. H., Spädtke, P., Wolf, B.: Proceedings of the Vth International Conference on the Physics of Highly-Charged Ions Giessen, 10.-14.9.1990, Z. Phys. D **21**, 205 (1991), ATOMIC PHYSICS OF HIGHLY-CHARGED IONS, Salzborn, E., Mokler, P. H., Müller, A. (eds.). Berlin, Heidelberg, New York: Springer 1991
14. Becker, R., Jennewein, E., Kleinod, M., Pröbstel, U., Valadkhani, K., Müller, A., Spies, W., Schennach, S., Angert, N., Bosch, F., Hofmann, I., Klabunde, J., Mokler, P. H., Schulte, H., Spädtke, P., Wolf, B.: Proceedings of the European Particle Accelerator Conference, Rom, 1988 EPAC 88, p. 607, Tazzari, S. (ed.). Singapore: World Scientific 1989
15. Kleinod, M., Becker, R., Jennewein, E., Pröbstel, U., Müller, A., Schennach, S., Haselbauer, J., Spies, W., Uwira, O., Wagner, M., Angert, N., Klabunde, J., Mokler, P. H., Spädtke, P., Wolf, B.: Proceedings of the Workshop on Electron Cooling and New Cooling Techniques, ECOOL 90, Legnaro, Italy, May 15.-17.1990, p. 230, Calabrese, R., Tecchio, L. (eds.). Singapore: World Scientific 1991
16. Kleinod, M., Becker, R., Jennewein, E., Pröbstel, U., Müller, A., Schennach, S., Haselbauer, J., Spies, W., Uwira, O., Wagner, M., Angert, N., Klabunde, J., Mokler, P. H., Spädtke, P., Wolf, B.: Proceedings of the 19th INS International Symposium on Cooler Rings and their Applications Tokyo, Japan, 5.-8.11.1990, pp. 258-264, Katayama, T., Noda, A. (eds.). Singapore: World Scientific 1991
17. Jennewein, E., Becker, R., Kleinod, M., Pröbstel, U., Müller, A., Schennach, S., Haselbauer, J., Spies, W., Uwira, O., Wagner, M., Angert, N., Klabunde, J., Mokler, P. H., Spädtke, P., Wolf, B.: Proceedings of the International Symposium on Heavy Ion Inertial Fusion Monterey, California, USA, 3.-6.12.1990, Particle Accelerators 37/38 (1992) 385-393
18. Becker, R., Jennewein, E.: Nucl. Instrum. Methods **A 258**, 503 (1987)
19. Müller, A.: Nucl. Instrum. Methods **A 282**, 80 (1989)
20. Poth, H.: Phys. Rep. **196**, 135 (1990)
21. Dittner, P. F., Datz, S., Miller, P. D., Moak, C. D., Stelson, P. H., Bottcher, C., Dress, W. B., Alton, G. D., Nešković, N.: Phys. Rev. Lett. **51**, 31 (1983)
22. Pierce, J. R.: Bell Syst. Techn. J. **30**, 825 (1951)
23. Herrmannsfeldt, W. B.: Stanford Linear Accelerator Laboratory Report SLAC 166 (1973); with modifications by Becker, R.
24. Stobbe, M.: Ann. Phys. **7**, 661 (1930)
25. Bethe, H., Salpeter, E.: Quantum Mechanics of One- and Two-Electron Systems. Berlin, Heidelberg, New York: Springer 1957
26. Frank, A., Müller, A., Haselbauer, J., Schennach, S., Spies, W., Uwira, O., Wagner, M., Becker, R., Jennewein, E., Kleinod, M., Angert, N., Mokler, P. H.: AIP Conference Proceedings 274, VIth International Conference on the Physics of Highly-Charged Ions Manhattan, Kansas, USA, 28.9.-2.10.1992, ATOMIC PHYSICS OF HIGHLY-CHARGED IONS, pp. 532-536, Richard, P., Stöckli, M., Cocke, C. L., Lin, C. D. (eds.). New York: American Institute of Physics 1993
27. Müller, A., Belić, D. S., DePaola, B. D., Djurić, N., Dunn, G. H., Mueller, D. W., Timmer, C.: Phys. Rev. **A 36**, 599 (1987)
28. Kanter, E. P., Schneider, D., Vager, Z., Gemmell, D. S., Zabransky, B. S., Yuan-zhuang, Gu, Arcuni, P., Koch, P. M., Mariani, D. R., Van de Water, W.: Phys. Rev. **A 29**, 583 (1984)
29. Hahn, Y.: Adv. At. Mol. Phys. **21**, 123 (1985)
30. Griffin, D. C., Pindzola, M. S., Bottcher, C.: Phys. Rev. **A 33**, 3124 (1986)
31. Badnell, N. R.: J. Phys. **B 19**, 3827 (1986)
32. Badnell, N. R., Pindzola, M. S.: Phys. Rev. **A 39**, 1685 (1989)

This article was processed by the author using the LaTeX style file *pljour2* from Springer-Verlag.